Energy & Environmental Science

PAPER

View Article Online
View Journal | View Issue

Cite this: *Energy Environ. Sci.*, 2016, **9**, 3221

Transition of lithium growth mechanisms in liquid electrolytes†

Peng Bai,*[a] Ju Li,[bc] Fikile R. Brushett[a] and Martin Z. Bazant*[ade]

Received 10th June 2016,
Accepted 8th August 2016

DOI: 10.1039/c6ee01674j

www.rsc.org/ees

Next-generation high-energy batteries will require a rechargeable lithium metal anode, but lithium dendrites tend to form during recharging, causing short-circuit risk and capacity loss, by mechanisms that still remain elusive. Here, we visualize lithium growth in a glass capillary cell and demonstrate a change of mechanism from root-growing mossy lithium to tip-growing dendritic lithium at the onset of electrolyte diffusion limitation. In sandwich cells, we further demonstrate that mossy lithium can be blocked by nanoporous ceramic separators, while dendritic lithium can easily penetrate nanopores and short the cell. Our results imply a fundamental design constraint for metal batteries ("Sand's capacity"), which can be increased by using concentrated electrolytes with stiff, permeable, nanoporous separators for improved safety.

Broader context

Consumer electronic devices, portable power tools, and electric vehicles have been enabled, but also constrained, by the steady improvement of lithium-ion batteries. To develop batteries with higher energy density, such as Li–O_2, Li–S, and other Li metal batteries using intercalation cathodes, lithium is believed to be the ideal anode material for its extremely high theoretical specific capacity (3860 mA h g^{-1}), low density (0.59 g cm^{-3}) and the lowest negative electrochemical potential (−3.04 V *vs.* the standard hydrogen electrode). Unfortunately, lithium growth is unstable during battery recharging and leads to rough, mossy deposits, whose fresh surfaces consume the electrolyte to form solid–electrolyte interphase layers, resulting in high internal resistance, low Coulombic efficiency and short cycle life. Finger-like lithium dendrites can also short-circuit the cell by penetrating the porous separator, leading to catastrophic accidents. Controlling such hazardous instabilities requires accurately determining their mechanisms, which are more complex than the well-studied diffusion-limited growth of copper or zinc from aqueous solutions. Such fundamental understanding is critical for the success of the lithium metal anode and could provide guidance for the optimal design and operation of rechargeable lithium metal batteries.

Introduction

The lithium metal anode is a key component of future high-energy batteries, such as Li–S and Li–O_2 batteries,[1] for economical and long-range electric vehicles.[2] It also holds the promise to reduce the volume and weight of lithium-ion batteries by replacing the standard graphite anode, if lithium dendrites can be safely controlled during recharging to avoid internal shorts and life-threatening accidents.[3] While it has been demonstrated that electrolyte additives,[4–6] artificial solid electrolyte interphase (SEI) layers,[7,8] and increasing the salt concentration in electrolytes,[9,10] either alone or in combination, can improve the stability of lithium under small currents[4–7] and low capacities,[9,11] the challenge of suppressing dendrites at practical currents (>1 mA cm^{-2}) and areal capacities (>1 mA h cm^{-2}) remains a major obstacle for the development of rechargeable lithium metal batteries.[8,12] The time is ripe for a thorough investigation of lithium growth mechanisms under these conditions, in order to establish theoretical principles and design constraints for dendrite-free charging.

The prevailing understanding of lithium growth instability is largely based on the simpler case of aqueous copper electrodeposition,[13–17] where dendritic fractal patterns are telltale signs of long-range diffusion-limited growth.[18–20] When a current is applied to recharge the battery, cations are consumed by reduction reaction, as anions are expelled by the electric field. In a binary

[a] *Department of Chemical Engineering, Massachusetts Institute of Technology, 77 Massachusetts Avenue, Cambridge, MA 02139, USA. E-mail: pengbai@mit.edu, bazant@mit.edu*
[b] *Department of Nuclear Science and Engineering, Massachusetts Institute of Technology, 77 Massachusetts Avenue, Cambridge, MA 02139, USA*
[c] *Department of Materials Science and Engineering, Massachusetts Institute of Technology, 77 Massachusetts Avenue, Cambridge, MA 02139, USA*
[d] *Department of Mathematics, Massachusetts Institute of Technology, 77 Massachusetts Avenue, Cambridge, MA 02139, USA*
[e] *Department of Materials Science and Engineering and SUNCAT Interfacial Science and Catalysis, Stanford University, Stanford, CA 94305, USA*

† Electronic supplementary information (ESI) available: Fig. S1 to S7, Tables S1 to S3, Movies S1 to S7 and additional references. See DOI: 10.1039/c6ee01674j

electrolyte, the evolution of neutral salt concentration obeys an effective diffusion equation.[21] For currents exceeding diffusion limitation, the salt concentration at the electrode surface decreases to zero at a characteristic time,[22,23] and uniform electroplating becomes unstable.[13,14,17] This characteristic time, t_{Sand}, was first derived by Sand in 1901,[22] and is now known as "Sand's time",[23] after which the scarce supply of cations preferentially deposits onto surface protrusions, leading to a self-amplifying process of dendritic growth (*i.e.* tip growth mode) that propagates at the velocity of bulk anion electromigration, in order to preserve electroneutrality.[13,17,21,24,25]

Attempts to transfer this understanding from copper to lithium have been inconclusive. In lithium/polymer-electrolyte cells,[26–28] the onset time for dendritic growth exhibits similar scaling with current as Sand's time, but surprisingly, far below the diffusion-limited current.[27] In lithium/liquid-electrolyte cells, decreasing the mobility and the transference number of anions by using modified separators can enhance the cycle life,[29] albeit again at currents well below the diffusion-limited current. Ramified moss-like or "mossy" deposits have even been observed at a current density of 10 μA cm^{-2} (ref. 30) and have been observed to grow from their roots,[31] rather than their tips, in contrast to all existing growth models. Moreover, the microscopic morphology of serpentine lithium filaments observed in various electrolytes,[3,5,9,32–35] over a range of length scales, do not resemble the branched, fractal structure of copper dendrites. These striking discrepancies between lithium and copper metal electrodeposition have lingered for decades without a clear explanation.

In this study, we aim to determine the precise conditions for short-inducing dendritic lithium to form, in order to establish design constraints for safe rechargeable metal batteries. We choose one of the most successful electrolytes for lithium-ion batteries,[36] $LiPF_6$ in the 1 : 1 mixture of ethylene carbonate (EC) and dimethyl carbonate (DMC), and conduct two sets of experiments to investigate the mechanisms of lithium dendrite growth under various conditions. The first experiments with novel capillary cells reveal that the relatively dense "mossy" lithium growth is reaction-limited and changes to fractal "dendritic" lithium in response to electrolyte diffusion limitation. The second experiments using sandwich cells demonstrate that root-growing mossy lithium can be blocked by a nanoporous ceramic membrane, while tip-growing dendritic lithium can easily penetrate the nanopores and cause the internal short only at over-limiting currents. Our results suggest that optimizing and monitoring the intrinsic transport properties of the battery could eliminate the formation of dendritic lithium and the risk of internal shorts thereafter.

Results

Transition from mossy to dendritic lithium

To better track the growth of lithium *in situ*, we fabricate a lithium|electrolyte|lithium symmetric cell in a special glass capillary, whose middle part is pulled thinner (Fig. 1a). A small piece of lithium metal is pushed into each end of the capillary until it lodges in the tapering part to seal the cell. Here, we are interested in the lithium deposition (reduction reaction), so the corresponding electrode should be called cathode. However, in order to be consistent with the convention of lithium metal anodes, we assume that the electrodeposition is a recharging process and the electrode is designated as an anode.

When a constant current is applied, moss-like lithium starts to deposit (Fig. 1c and d), and the salt concentration near the surface starts to decrease,[37] as indicated by the gradually increasing voltage (Fig. 1b). After ~40 min of polarization, the voltage starts to diverge upon salt depletion at the anode surface,[38] and a wispy dendrite suddenly shoots out (at 2678s in Fig. 1e) in an obvious tip-growing manner, leaving behind stagnant mossy lithium. The dendrite's fractal structure remains the same after two weeks of relaxation.

The striking differences in morphology and dynamics imply two different mechanisms, switching from reaction-limited to transport-limited growth at the voltage spike. In the early stages of electrodeposition, mossy lithium mainly grows from its roots, as revealed by the movement of the tips, which barely change shape as they are pushed forward (ESI,† Fig. S1 and Movies S1, S2). Root growth has also been observed by Yamaki *et al.*[31] below the limiting current and attributed to internal stress release beneath the SEI layer on the lithium electrode. While growing into the open electrolyte, the mossy lithium also thickens, and the process has been described vividly as "rising dough".[30] It is noteworthy that at the microscopic scale, the relatively dense moss-like structure is composed of whiskers, although the width of an individual whisker varies in different electrolytes.[5,9,30,35] Such random surface growth is typical of reaction-limited deposition.[19] Compared with copper electrodeposition,[14] the key difference is that lithium, covered by SEI, develops whiskers and mossy structures, while copper, without SEI, forms whisker-free yet compact deposition before Sand's time.[39] Due to the insulating SEI that forms on individual lithium whiskers, mossy lithium is unable to transform into a uniform metallic film through a ripening process, even under mechanical pressure. At the voltage spike, sparse lithium dendrites grow explosively from their tips with the fractal morphology of diffusion-limited aggregation,[19] also shared by copper dendrites,[13,14] because electrodeposition is in the same universality class.[40,41] The similarity between lithium and copper dendrites implies that both metals have similar surface tension, so the formation of dendritic lithium is correlated with the lack of lithium salt to form SEI different from that of mossy lithium, or very little SEI until the concentration relaxes after the initial burst of growth.

To test the hypothesis of diffusion limitation, the experimental times to reach the voltage spike are used to calculate an apparent diffusion coefficient D_{app} from Sand's formula,[22]

$$t_{Sand} = \pi D_{app} \frac{(z_c c_0 F)^2}{4(J t_a)^2} \quad (1)$$

where z_c is the charge number of the cation (z_c = 1 for Li^+), c_0 is the bulk salt concentration, F is the Faraday's constant,

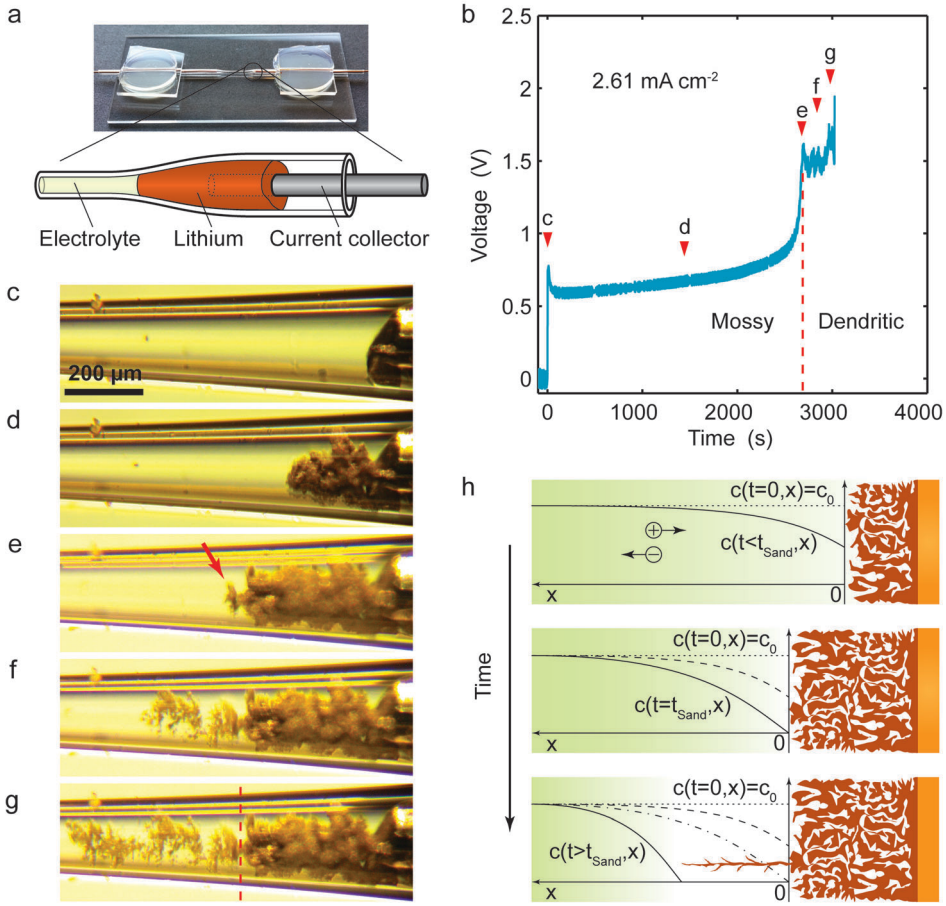

Fig. 1 *In situ* observations of lithium electrodeposition in a glass capillary filled with an electrolyte solution consisting of 1 M $LiPF_6$ in EC/DMC. (a) Photo of the capillary cell, whose middle part was pulled thinner for easier optical observation. (b) Voltage responses of the capillary cell at a deposition current density of 2.61 mA cm^{-2}. (c–g) *In situ* snapshots of the growth of lithium during the electrodeposition. Red arrow in (e) points to the emergence of dendritic lithium. Red dash line in (g) labels the clear morphological difference between the pre- and post-Sand's time lithium deposits. (h) Theoretical interpretation of the growth mechanisms of lithium electrodeposition during concentration polarization.

J is the current density, and t_{Li} = 0.38 and $t_a = 1 - t_{Li}$ are the transference numbers of lithium cations and associated anions. For c_0 = 1 M, the calculated value, $D_{app} = 1.0 \times 10^{-6}$ cm^2 s^{-1}, is consistent with reported values 3.0–3.5 $\times$ 10^{-6} cm^2 s^{-1} for small-current relaxation.[42,43] As shown in Fig. 2a, the voltage spike at Sand's time is consistently observed above the limiting current density, $J_{lim} = 2z_c c_0 F D_{app}(t_a L)^{-1} \approx 1$ mA cm^{-2}, where $L \approx 5$ mm is the distance between the electrodes. With the aid of the *in situ* snapshots (Fig. 2b), we accurately measured the "experimental Sand's time" for the onset of dendrites at each current density. The log–log plot can be fitted with a slope of −1.40 (Fig. 2c). Scaling exponents > -2 have also been reported (without explanation) for the short-circuiting time in other lithium cells.[44] As shown in the ESI,† the deviation observed here is attributable to convection by electro-osmotic flow in the depleted zone,[45,46] although other effects, such as spatially varying porosity and/or deposit morphology, can also lead to different scaling laws for propagating diffusion layers in porous media.[47]

As a new battery relevant metric, we convert Sand's time into "Sand's capacity" by multiplying with the current density. The plot of Sand's capacity *versus* current density (Fig. 2d) provides a simple design constraint to avoid dendritic lithium. Interestingly, most state-of-the-art lithium metal anodes do not operate in the regime of dendritic lithium identified by the capillary cell, which is already much lower than that of the sandwich cells. Since the growth mechanism switches by diffusion limitation, absolute current densities cannot be meaningfully compared across different cells. It is the relative current density, with respect to the system-specific limiting current, that controls the transition from mossy to dendritic lithium.

Blockage of mossy lithium

We then apply the knowledge of growth mechanisms from the capillary cell to investigate the ability of a nanoporous separator to block mossy and dendritic lithium in a battery relevant sandwich cell. Since the smallest known whiskers in mossy lithium are ~1 μm thick,[3] we construct the cell using an anodic aluminum oxide (AAO) membrane with submicron pores (<200 nm), to see whether the mossy lithium can be blocked (Fig. 3a).

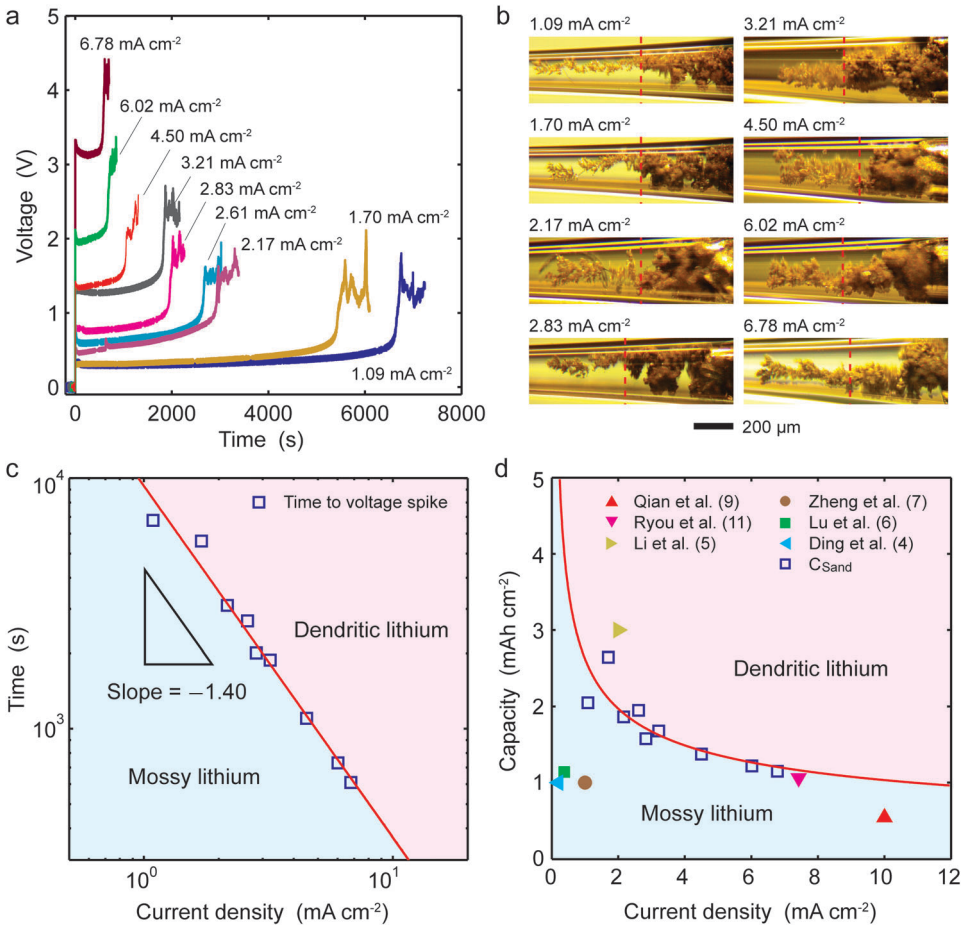

Fig. 2 Change of growth mechanism at Sand's time during concentration polarization. (a) Voltage responses of capillary cells at various deposition current densities. (b) Representative optical images of lithium deposits demonstrating the clear change of morphologies at Sand's time for various current densities. (c) Log–log plot of the experimental Sand's times for various current densities. (d) Current-dependent Sand's capacity with previous reports shown.

Based on the electrode separation, 300 μm, the limiting current density for the sandwich cell is approximately 20 mA cm^{-2}. When an under-limiting current density of 10 mA cm^{-2} is applied, the voltage stabilizes at 0.2 V and lasts for a capacity well beyond the pure lithium limit that the compartment below the AAO can accommodate (Fig. 3a), indicating some deformation of the membrane. After dissembling the cell, an intact, free-standing AAO membrane is recovered with a dense lithium disk below it (Fig. S5, ESI†), which confirms the complete blockage of mossy lithium growth. Surprisingly, even when the AAO membrane is pressed in direct contact with the lithium metal anode, a significant amount of porous lithium can still be deposited below the AAO, as shown in Fig. 3c and d. The mossy lithium shown in the SEM images is clearly too bulky to penetrate AAO, and only forms a space-filling porous layer between the electrode and the separator, reducing the risk of short circuit below the limiting current. These results help explain why various ceramic membranes can prevent lithium short circuits,[6,44,48,49] especially under normal conditions (<10 mA cm^{-2}), where only the dense root-growing mossy lithium is developed in the cell.

As demonstrated in the capillary cell experiments, once Sand's capacity is exceeded, dendritic lithium suddenly appears. When an over-limiting current density of 50 mA cm^{-2} is applied to the sandwich cell, the voltage quickly increases and leads to a short circuit. As revealed by the SEM images, very thin lithium filaments can now be found among mossy deposits on the anode side (Fig. 3e and f). Clusters of granular deposits, smaller than the pores of AAO, are also clearly visible on the cathode side (Fig. 3g and h), which confirm that lithium penetration through the ceramic nanopores caused the short circuit. The stark difference between mossy and dendritic lithium deposits leads us to propose that the term "dendrite" be used more narrowly, only to describe a fractal, tip-growing deposit resulting from diffusion-limited growth, consistent with the well-studied copper and zinc dendrites. If lithium dendrite penetration in AAO were mainly opposed by surface tension, then the breakthrough voltage (where the overpotential exceeds the Young–Laplace pressure) would scale with the inverse of the pore size.[50] The dendrite penetration may be further suppressed by modifying the surface charge of the nanopores,[15] when over-limiting mass transfer is opposed by surface conduction.[46]

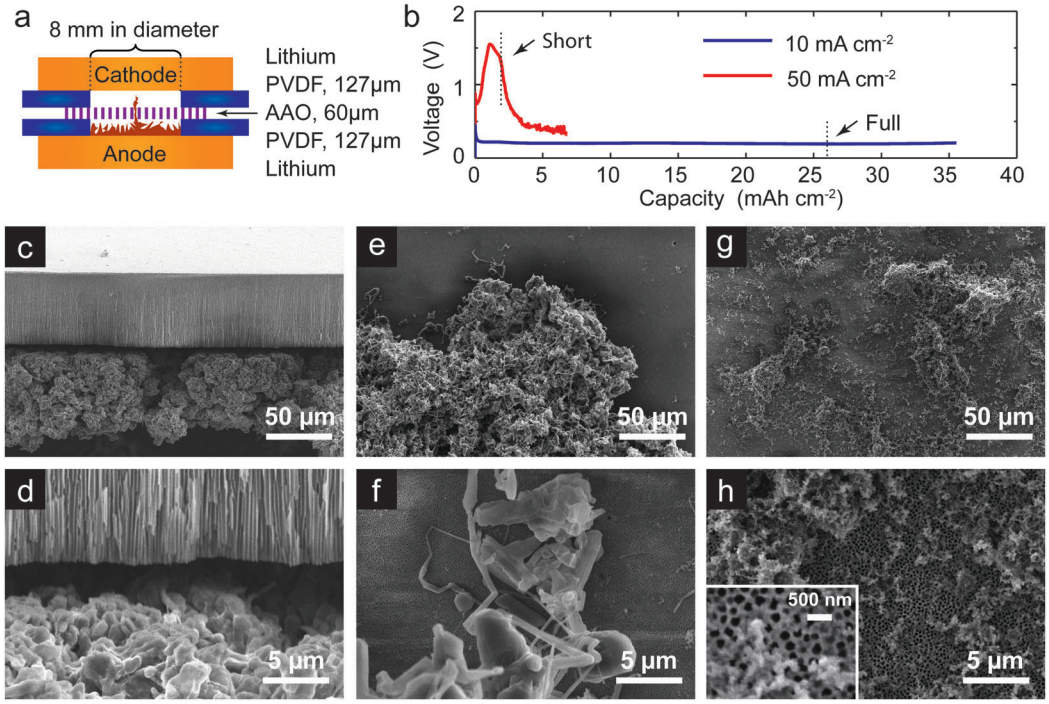

Fig. 3 Lithium electrodeposition in sandwich cells. (a) Structure of the symmetric sandwich cell, where names of the electrodes follow the convention of lithium batteries, *i.e.* lithium deposits onto the anode during recharging. (b) Voltage responses of the sandwich cells, indicating the complete blockage of lithium deposits even beyond the theoretical capacity of the lower compartment at 10 mA cm^{-2}, as well as the quick penetration of AAO and short-circuiting of the cell at 50 mA cm^{-2}. (c and d) Scanning electron microscopy (SEM) images of the AAO/Li-deposit interface, revealing the blockage of bulky porous lithium formed in the under-limiting current conditions. (e and f) SEM images of the anode-facing side of AAO, displaying both bulky and needle-like lithium deposits formed in the over-limiting current conditions. (g and h) SEM images of the cathode-facing side of AAO, showing nanosized lithium deposits coming out of the nanopores of AAO. Inset: Magnification of the clusters of granular lithium deposits around the pores of AAO (appear as black dots).

Sand's capacity as the safety limit

Our results reveal why the risk of dendrites increases with aging, and how to mitigate it. According to the definition of Sand's capacity,

$$C_{\text{Sand}} = Jt_{\text{Sand}} = \pi D_{\text{app}} \frac{(z_c c_0 F)^2}{4Jt_a^2} \quad (2)$$

dilution of the electrolyte alone could significantly lower the safety limit, which is verified experimentally with our capillary cells by varying the salt concentration c_0 (Fig. 4). In practical cells, the cycling of mossy lithium consumes a large amount of the liquid electrolyte (salt and solvent) to form SEI layers.[8,12,51,52] This lowers the amount of the dissolved lithium salt, and thereby the effective diffusivity D_{app}, which not only results in higher impedance, but also steadily lowers the intrinsic Sand's capacity. While the high impedance has been identified in a few experiments as a major cause of battery failure,[8,9,12,51] dendritic lithium can still develop and short aged cells when using 1 M electrolyte,[9] where the decrease of the intrinsic Sand's capacity below the cycled capacity could be an explanation. Therefore, increasing Sand's capacity by increasing the salt concentration in the electrolyte should be an effective method to improve the safety of rechargeable metal batteries. Interestingly, highly concentrated electrolytes have already enabled very high Coulombic efficiency,[9,10,35] which is beneficial to longer cycle life.

Dimensionless safety criterion

In order to compare different systems and make general scaling predictions about the safety limit, we employ dimensional analysis. Following earlier definitions, L is the distance between the two electrodes, then $L/2$ is a characteristic length scale for electrolyte diffusion with apparent diffusivity D_{app}, *i.e.* the distance from the electrode (where salt depletion occurs) to a reservoir at concentration c_0. Let J_{lim} be the steady-state diffusion-limited current, and C_{Sand} be the maximum (Sand's) areal capacity for safe operation at a given current density J. If these are the only important parameters, then, simply as a consequence of their physical units, Buckingham's theorem[53] states that there must exist a scaling relation $\tilde{C}_{\text{Sand}} = f(\tilde{J})$ between the dimensionless Sand's capacity and the dimensionless applied current density,

$$\tilde{C}_{\text{Sand}} = \frac{4C_{\text{Sand}}D_{\text{app}}}{JL^2} \quad (3)$$

$$\tilde{J} = \frac{J}{J_{\text{lim}}} \quad (4)$$

Substitution of eqn (2) and (4) into eqn (3), with the limiting current density for the dilute binary electrolyte, $J_{\text{lim}} = 2z_c c_0 F D_{\text{app}}(t_a L)^{-1}$, yields the scaling function,

$$\tilde{C}_{\text{Sand}} = f_{\text{dilute}}(\tilde{J}) = \frac{\pi}{4\tilde{J}^2} \quad (5)$$

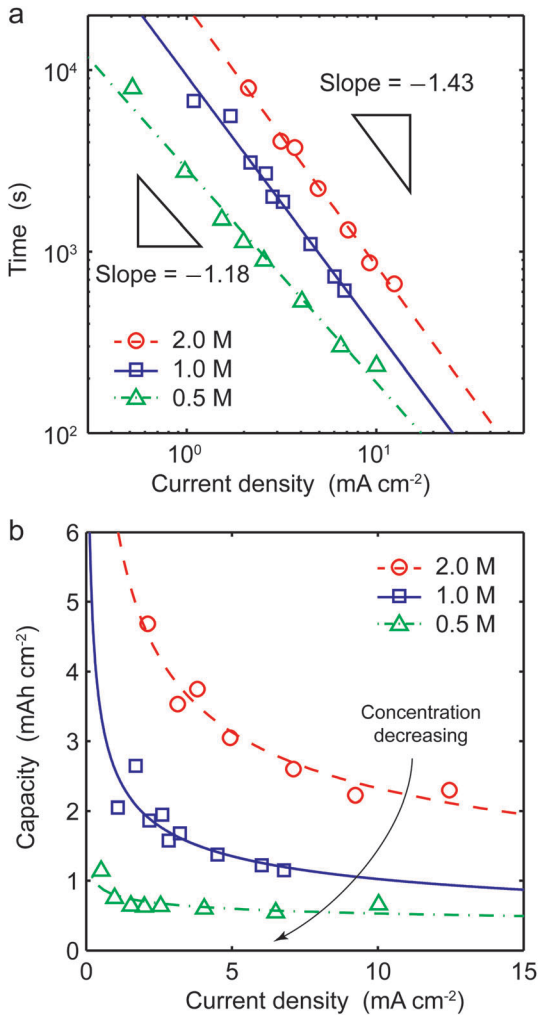

Fig. 4 Concentration-dependent Sand's behavior. Experimental (a) Sand's times and (b) Sand's capacities for 0.5 M and 2 M electrolytes, with results of 1 M electrolyte from Fig. 2 as references.

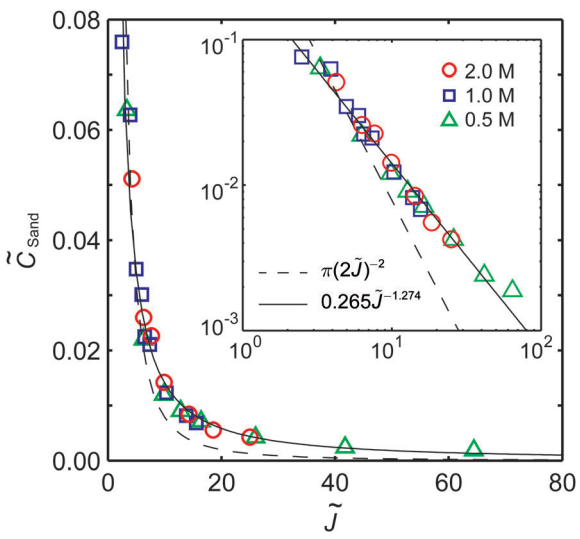

Fig. 5 Linear and logarithmic (inset) plots of dimensionless Sand's capacity *versus* dimensionless current density. Dashed line is the prediction of Sand's formula for dilute electrolytes, while solid line is the best fit to the experimental data.

The same scaling function governs the time, $t_{Sand} = C_{Sand} J^{-1}$, required to reach Sand's capacity at constant current, scaled to the diffusion time: $\tilde{t}_{Sand} = 4t_{Sand}D_{app}L^{-2} = f(\tilde{J})$, which can also be derived by solving the ambipolar diffusion equation for transient overlimiting current density $\tilde{J} > 1$ (ESI†).

The scaling function will differ for concentrated electrolytes[54] (with concentration-dependent diffusivities and coupled Stefan–Maxwell fluxes) in porous separators[47] (with possibly variable porosity and tortuosity, surface conduction and electro-osmotic flows), but the trend should be the same as predicted by dilute solution theory.[55] When the experimental data shown in Fig. 4b are nondimensionalized with corresponding D_{app} (Table S3, ESI†) and plotted in Fig. 5 as $\tilde{C}_{Sand}$ *versus* $\tilde{J}$, a reasonable data collapse is observed, similar to the dilute solution prediction, eqn (5), but with a modified scaling function, $f(\tilde{J}) = 0.265\tilde{J}^{-1.274}$, which is mainly attributable to electro-osmotic convection in the capillary cells (Fig. S4, ESI†).

Discussion

Our results suggest that monitoring the capacity loss and transient responses to estimate transport properties and the associated Sand's capacity could enable battery management systems to avoid dendrites by adjusting the applied current or cycled capacity windows in real time, which is particularly important for rechargeable lithium metal batteries cycling at high capacities. This prediction may seem at odds with the fact that some Li–S prototypes can be cycled at a very large specific capacity for hundreds of times without signs of internal shorts. There is no contradiction, however, after accounting for capacity differences. By multiplying the specific capacity with the small loading mass of the active sulfur,[56] the converted areal capacity (in units of mA h cm^{-2}) that matters for the metal anode is actually smaller than those of mature lithium-ion batteries.[56,57] For future rechargeable lithium metal batteries that possess a high specific energy with respect to the total mass, and operate at a truly large areal capacity, on-board diagnosis of the intrinsic Sand's capacity of the battery to avoid dendritic lithium may become a practical solution for safe operation, before a robust chemistry that can completely suppress the continuous consumption of electrolyte (due to the growth of lithium whiskers) is developed.

Carbonate-base electrolytes, such as what we use in this work, are known to effect relatively thin lithium whiskers.[32] Ether-based electrolytes, in contrast, allow lithium whiskers to grow much thicker.[7–9,58,59] At a given areal capacity, thicker lithium whiskers create less surface area and therefore consume less lithium salt and solvent to develop SEI layers. In addition, fluorosulfonate species used in these electrolytes, such as lithium bis(trifluoromethane-sulphonyl)imide (LiTFSI) and lithium bis(fluorosulfonyl)imide (LiFSI), could undergo extensive reactions with lithium to form a robust LiF-rich SEI,[52,59] which could also be facilitated by employing very high salt concentrations.[9] However, whether the SEI layers formed in ether-based electrolytes will remain stable during cycling at larger areal capacities, and thereby

retard the continuous consumption of electrolytes[12,60] to retain high Coulombic efficiency and long cycle life is yet to be verified experimentally. Investigating the fundamental mechanisms alongside may help engineer better SEI in other high-voltage solvents,[36,61] with which the standard graphite anode in lithium-ion batteries may be replaced by ultrathin lithium metal anodes or simply removed to double the energy density. Of course, the chemistry of SEI does not override transport processes in electrolytes. Transitions from root-growing mossy lithium to tip-growing dendritic lithium also occur in ether-based electrolytes (Fig. S7 and Movie S6, S7, ESI†).

An important implication of our study is the need for consistent terminology, not only to refer to the different lithium morphologies, but also to clarify the underlying mechanisms for rational battery design and engineering. Comparing various published work with ours, the thin needle-like lithium filaments that grow from their roots below the limiting current should be called "whiskers", which interweave with each other to form a "mossy" structure as the capacity increases. In contrast, the widely-used term "dendrites" should be reserved for the classical branched fractal structures that grow at their tips, which only occur at diffusion limitation and cannot revert to form a mossy structure. Although individual whiskers in the mossy structure may become thinner or disconnected over many deposition/dissolution cycles, as long as the current density remains under-limiting, the root-growth mechanism will make penetrating ceramic nanopores as difficult as threading a needle. With further investigations of SEI formation on mossy lithium and its interaction with ceramic separators during cycling, an ultimate safe solution should be possible.

Conclusions

While the failure mechanisms in practical batteries with opaque separators are still challenging to investigate *in situ*,[62] our capillary cells provide a simple and effective means to explore the hidden physics. We have demonstrated that lithium growth in liquid electrolytes follows two different mechanisms, depending on the applied current and capacity. Below Sand's capacity, reaction-limited mossy lithium mainly grows from the roots and cannot penetrate hard ceramic nanopores in a sandwich cell. Above Sand's capacity, transport-limited dendritic lithium grows at the tips and can easily cross the separator to short the cell. Our results suggest maximizing Sand's capacity by increasing the salt concentration in the electrolyte. Electrolyte degradation should also be monitored to prevent dendrites by keeping the cycled capacity below Sand's capacity. Ceramic separators with pores smaller than mossy lithium whiskers could replace conventional polyolefin separators with flexible large pores to enhance safety and cycle life, and the effect could be further reinforced with lithium salts and solvents that favor thicker columnar deposits. To the broader field of electrodeposition, our results clarify the physical connections between lithium and copper/zinc dendrites formed in liquid electrolytes. Mechanisms and mathematical models of copper/zinc dendrite growths cannot be and should not be applied to explain either the development or the suppression of lithium whiskers. Future theoretical investigations should take into account the dynamics of SEI formation during both the root-growth and tip-growth processes of lithium electrodeposition.

Methods

Materials

The battery grade electrolyte (1 M $LiPF_6$ in ethylene carbonate/dimethyl carbonate with a volume ratio of 1 : 1), ethylene carbonate (EC, anhydrous, 99%), dimethyl carbonate (DMC, anhydrous, $\geq$99%), and Whatman AAO membranes (pore size 100 nm, thickness 60 μm, diameter 13 mm) were purchased from Sigma-Aldrich, and used as received. Lithium bis-(trifluoromethane-sulphonyl)imide (LiTFSI), 1,3-dioxolane (DOL) and 1,2-dimethoxyethane (DME) were purchased from BASF Corporation. Lithium bis(fluorosulfonyl)imide (LiFSI) was purchased from Oakwood Products Inc. Copper wires, stainless steel wires, and polyvinylidene fluoride (PVDF) sheets were purchased from McMaster-Carr. The glass capillaries were purchased from Narishige Co., Ltd. Lithium chips (99.9%, thickness 250 μm, diameter 15.6 mm) were purchased from MTI Corporation.

Cell fabrication and electrochemical testing

The glass capillaries were pulled 7 mm longer with a vertical type micropipette puller (PC-10, Narishige Co., Ltd). The pulled capillary was bonded onto a glass slide with silicone and then transferred into the Argon-filled glovebox. To avoid gas bubbles, the electrolyte was filled in only by the capillary effect. Then, a small piece of lithium metal was pushed into each end of the cell by a metal wire to clog at the tapering part of the capillary to seal the cell. Separation between the lithium electrodes is around 5 mm for all cells. Sandwich cells were constructed in the split test cells purchased from MTI Corporation. A piece of lithium chip was first gently pressed onto the bottom part of the cell and covered by a customized PVDF washer punched off from the PVDF sheet. Several drops of electrolyte were dispensed on the surface of lithium, which also immerse the PVDF washer. A piece of AAO was then carefully placed on top of the PVDF washer and covered by another piece of PVDF washer. A few more drops of electrolyte were dispensed on AAO until the second PVDF washer is immersed. Finally the second lithium chip was stacked on top of the second PVDF, and then covered by a stainless steel disk. The whole cell was assembled together with the upper part (spring-loaded) of the test cell. Electrochemical tests were conducted with an Arbin battery tester (BT 2043, Arbin Instruments). *In situ* images were captured by an optical microscope (MU500, AmScope). All experiments were performed at room temperature in an Argon-filled glovebox (Vigor Tech USA) with water and oxygen content less than 1 ppm.

SEM characterization

AAO separators with lithium deposits harvested from sandwich cells were washed with DMC for three times, then fixed onto the

SEM sample holders with carbon adhesive and sealed in an air-tight box before moving out of the Argon-filled glovebox. The residual DMC on the samples helps protect the lithium from the ambient atmosphere when transferring them into the chamber of the Analytical Scanning Electron Microscope (JEOL, 6010LA), which usually takes less than 10 s before the vacuum evacuation.

Acknowledgements

This work is supported by Robert Bosch LLC through the MIT Energy Initiative (MITei). P. B. thanks Mr William DiNatale in the Institute for Soldier Nanotechnologies at MIT for providing the access to the micropipette puller. J. L. acknowledges support by NSF DMR-1410636. M. Z. B. acknowledges support from the Global Climate and Energy Project at Stanford University and by the US Department of Energy, Basic Energy Sciences through the SUNCAT Center for Interface Science and Catalysis. The authors thank Dr Sarah Stewart for helpful discussions.

Notes and references

1 P. G. Bruce, S. A. Freunberger, L. J. Hardwick and J. M. Tarascon, *Nat. Mater.*, 2012, **11**, 19–29.
2 J. M. Tarascon and M. Armand, *Nature*, 2001, **414**, 359–367.
3 W. Xu, J. Wang, F. Ding, X. Chen, E. Nasybulin, Y. Zhang and J.-G. Zhang, *Energy Environ. Sci.*, 2014, **7**, 513–537.
4 F. Ding, W. Xu, G. L. Graff, J. Zhang, M. L. Sushko, X. L. Chen, Y. Y. Shao, M. H. Engelhard, Z. M. Nie, J. Xiao, X. J. Liu, P. V. Sushko, J. Liu and J. G. Zhang, *J. Am. Chem. Soc.*, 2013, **135**, 4450–4456.
5 W. Y. Li, H. B. Yao, K. Yan, G. Y. Zheng, Z. Liang, Y. M. Chiang and Y. Cui, *Nat. Commun.*, 2015, **6**, 7436.
6 Y. Y. Lu, Z. Y. Tu and L. A. Archer, *Nat. Mater.*, 2014, **13**, 961–969.
7 G. Y. Zheng, S. W. Lee, Z. Liang, H. W. Lee, K. Yan, H. B. Yao, H. T. Wang, W. Y. Li, S. Chu and Y. Cui, *Nat. Nanotechnol.*, 2014, **9**, 618–623.
8 D. Aurbach, E. Zinigrad, H. Teller and P. Dan, *J. Electrochem. Soc.*, 2000, **147**, 1274–1279.
9 J. F. Qian, W. A. Henderson, W. Xu, P. Bhattacharya, M. Engelhard, O. Borodin and J. G. Zhang, *Nat. Commun.*, 2015, **6**, 6362.
10 L. Suo, Y.-S. Hu, H. Li, M. Armand and L. Chen, *Nat. Commun.*, 2013, **4**, 1481.
11 M. H. Ryou, Y. M. Lee, Y. J. Lee, M. Winter and P. Bieker, *Adv. Funct. Mater.*, 2015, **25**, 834–841.
12 D. Aurbach, E. Zinigrad, Y. Cohen and H. Teller, *Solid State Ionics*, 2002, **148**, 405–416.
13 V. Fleury, M. Rosso, J. N. Chazalviel and B. Sapoval, *Phys. Rev. A: At., Mol., Opt. Phys.*, 1991, **44**, 6693–6705.
14 J. Elezgaray, C. Leger and F. Argoul, *J. Electrochem. Soc.*, 1998, **145**, 2016–2024.
15 J.-H. Han, E. Khoo, P. Bai and M. Z. Bazant, *Sci. Rep.*, 2014, **4**, 7056.
16 R. M. Brady and R. C. Ball, *Nature*, 1984, **309**, 225–229.
17 C. Leger, J. Elezgaray and F. Argoul, *Phys. Rev. E: Stat. Phys., Plasmas, Fluids, Relat. Interdiscip. Top.*, 1998, **58**, 7700–7709.
18 T. A. Witten and L. M. Sander, *Phys. Rev. Lett.*, 1981, **47**, 1400–1403.
19 A.-L. s. Barabási and H. E. Stanley, *Fractal concepts in surface growth*, Press Syndicate of the University of Cambridge, New York, NY, USA, 1995.
20 A. Bunde and S. Havlin, *Fractals and disordered systems*, Springer, Berlin, New York, 1996.
21 J. S. Newman and K. E. Thomas-Alyea, *Electrochemical systems*, J. Wiley, Hoboken, NJ, 2004.
22 H. J. S. Sand, *Philos. Mag.*, 1901, **1**, 45–79.
23 A. J. Bard and L. R. Faulkner, *Electrochemical methods: fundamentals and applications*, Wiley, New York, 2001.
24 D. P. Barkey and P. D. Laporte, *J. Electrochem. Soc.*, 1990, **137**, 1655–1656.
25 M. Z. Bazant, *Phys. Rev. E: Stat. Phys., Plasmas, Fluids, Relat. Interdiscip. Top.*, 1995, **52**, 1903–1914.
26 C. Brissot, M. Rosso, J. N. Chazalviel and S. Lascaud, *J. Power Sources*, 1999, **81–82**, 925–929.
27 M. Rosso, T. Gobron, C. Brissot, J. N. Chazalviel and S. Lascaud, *J. Power Sources*, 2001, **97–98**, 804–806.
28 M. Rosso, C. Brissot, A. Teyssot, M. Dolle, L. Sannier, J. M. Tarascon, R. Bouchetc and S. Lascaud, *Electrochim. Acta*, 2006, **51**, 5334–5340.
29 Z. Y. Tu, P. Nath, Y. Y. Lu, M. D. Tikekar and L. A. Archer, *Acc. Chem. Res.*, 2015, **48**, 2947–2956.
30 J. Steiger, D. Kramer and R. Moenig, *Electrochim. Acta*, 2014, **136**, 529–536.
31 J. Yamaki, S. Tobishima, K. Hayashi, K. Saito, Y. Nemoto and M. Arakawa, *J. Power Sources*, 1998, **74**, 219–227.
32 F. Ding, W. Xu, X. L. Chen, J. Zhang, M. H. Engelhard, Y. H. Zhang, B. R. Johnson, J. V. Crum, T. A. Blake, X. J. Liu and J. G. Zhang, *J. Electrochem. Soc.*, 2013, **160**, A1894–A1901.
33 R. R. Miao, J. Yang, Z. X. Xu, J. L. Wang, Y. Nuli and L. M. Sun, *Sci. Rep.*, 2016, **6**, 21771.
34 Z. Li, J. Huang, B. Y. Liaw, V. Metzler and J. B. Zhang, *J. Power Sources*, 2014, **254**, 168–182.
35 R. Cao, J. Chen, K. S. Han, W. Xu, D. Mei, P. Bhattacharya, M. H. Engelhard, K. T. Mueller, J. Liu and J.-G. Zhang, *Adv. Funct. Mater.*, 2016, **26**, 3059–3066.
36 K. Xu, *Chem. Rev.*, 2004, **104**, 4303–4417.
37 H. J. Chang, A. J. Ilott, N. M. Trease, M. Mohammadi, A. Jerschow and C. P. Grey, *J. Am. Chem. Soc.*, 2015, **137**, 15209–15216.
38 C. Brissot, M. Rosso, J. N. Chazalviel and S. Lascaud, *J. Electrochem. Soc.*, 1999, **146**, 4393–4400.
39 K. I. Popov, S. S. Djokic and B. N. Grgur, *Fundamental aspects of electrometallurgy*, Kluwer Academic/Plenum Publishers, New York, 2002.
40 M. Z. Bazant, *Proc. R. Soc. A*, 2004, **460**, 1433–1452.
41 M. Z. Bazant, J. Choi and B. Davidovitch, *Phys. Rev. Lett.*, 2003, **91**, 045503.
42 L. O. Valoen and J. N. Reimers, *J. Electrochem. Soc.*, 2005, **152**, A882–A891.

43 A. Nyman, M. Behm and G. Lindbergh, *Electrochim. Acta*, 2008, **53**, 6356–6365.
44 S. Choudhury, R. Mangal, A. Agrawal and L. A. Archer, *Nat. Commun.*, 2015, **6**, 10101.
45 J. M. Huth, H. L. Swinney, W. D. Mccormick, A. Kuhn and F. Argoul, *Phys. Rev. E: Stat. Phys., Plasmas, Fluids, Relat. Interdiscip. Top.*, 1995, **51**, 3444–3458.
46 E. V. Dydek, B. Zaltzman, I. Rubinstein, D. S. Deng, A. Mani and M. Z. Bazant, *Phys. Rev. Lett.*, 2011, **107**, 118301.
47 A. Mani and M. Z. Bazant, *Phys. Rev. E: Stat., Nonlinear, Soft Matter Phys.*, 2011, **84**, 061504.
48 Y.-k. Ahn, J. Park, D. Shin, S. Cho, S. Y. Park, H. Kim, Y. Piao, J. Yoo and Y. S. Kim, *J. Mater. Chem. A*, 2015, **3**, 10715–10719.
49 Z. Tu, Y. Kambe, Y. Lu and L. A. Archer, *Adv. Energy Mater.*, 2014, **4**, 1300654.
50 A. Jana, D. R. Ely and R. E. Garcia, *J. Power Sources*, 2015, **275**, 912–921.
51 D. P. Lv, Y. Y. Shao, T. Lozano, W. D. Bennett, G. L. Graff, B. Polzin, J. G. Zhang, M. H. Engelhard, N. T. Saenz, W. A. Henderson, P. Bhattacharya, J. Liu and J. Xiao, *Adv. Energy Mater.*, 2015, **5**, 1400993.
52 X. B. Cheng, R. Zhang, C. Z. Zhao, F. Wei, J. G. Zhang and Q. Zhang, *Adv. Sci.*, 2016, **3**, 1500213.
53 G. I. Barenblatt, *Dimensional analysis*, Gordon and Breach Science Publishers, New York, 1987, pp. 31–48.
54 S. A. Mareev, D. Y. Butylskii, A. V. Kovalenko, A. V. Petukhova, N. D. Pismenskaya, L. Dammak, C. Larchet and V. V. Nikonenko, *Electrochim. Acta*, 2016, **195**, 85–93.
55 M. Z. Bazant, *10.626 Electrochemical Energy Systems (Spring 2014)*, Massachusetts Institute of Technology: MIT OpenCourseWare, http://ocw.mit.edu. License: Creative Commons BY-NC-SA.
56 M. Hagen, D. Hanselmann, K. Ahlbrecht, R. Maca, D. Gerber and J. Tubke, *Adv. Energy Mater.*, 2015, **5**, 1401986.
57 H. H. Zheng, J. Li, X. Y. Song, G. Liu and V. S. Battaglia, *Electrochim. Acta*, 2012, **71**, 258–265.
58 J. Steiger, G. Richter, M. Wenk, D. Kramer and R. Monig, *Electrochem. Commun.*, 2015, **50**, 11–14.
59 R. R. Miao, J. Yang, X. J. Feng, H. Jia, J. L. Wang and Y. N. Nuli, *J. Power Sources*, 2014, **271**, 291–297.
60 D. Aurbach, Y. Talyosef, B. Markovsky, E. Markevich, E. Zinigrad, L. Asraf, J. S. Gnanaraj and H. J. Kim, *Electrochim. Acta*, 2004, **50**, 247–254.
61 K. Xu, *Chem. Rev.*, 2014, **114**, 11503–11618.
62 K. J. Harry, D. T. Hallinan, D. Y. Parkinson, A. A. MacDowell and N. P. Balsara, *Nat. Mater.*, 2014, **13**, 69–73.

Electronic Supplementary Information for

Transition of lithium growth mechanisms in liquid electrolytes

Peng Bai[a,*], Ju Li[b,c], Fikile R. Brushett[a], Martin Z. Bazant[a,d,e,*]

Departments of [a]Chemical Engineering, [b]Nuclear Science and Engineering, [c]Materials Science and Engineering and [d]Mathematics, Massachusetts Institute of Technology, 77 Massachusetts Avenue, Cambridge, MA 02139, USA

[e]Department of Materials Science and Engineering and SUNCAT Interfacial Science and Catalysis, Stanford University, Stanford, CA 94305, USA

*Correspondence to: pengbai@mit.edu, bazant@mit.edu

This file includes:

Supplementary text with

Figs. S1 to S7

Tables S1 to S3

References (63-64)

Other Supplementary Materials for this manuscript includes the following:

Movies S1 to S7

Growth of mossy lithium before Sand's time

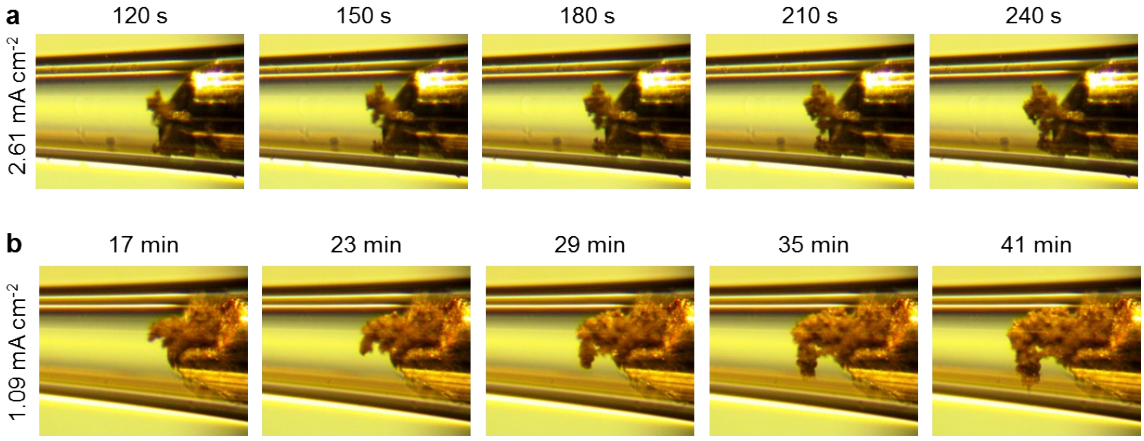

Figure S1. Visualization of the root-growth mechanism of mossy lithium before Sand's time. While the deposits continuously thicken themselves globally, the (a) displacement and (b) rotation of the tips reveal that major proliferations occur at locations behind the tips, which is a stark difference from existing models of transport-limited growth occurring only at the tips.

Calculation of the current densities

Since the Sand's time and the instability occurred on the surface of the electrode are all determined by the depletion of the electrolyte, the current density in Sand's formula should be the flux density through the cross-section of the capillary, not the local current density on the electrode, so we measured the inner diameter of the capillary to determine the area (Fig. S2), based on which current density is calculated.

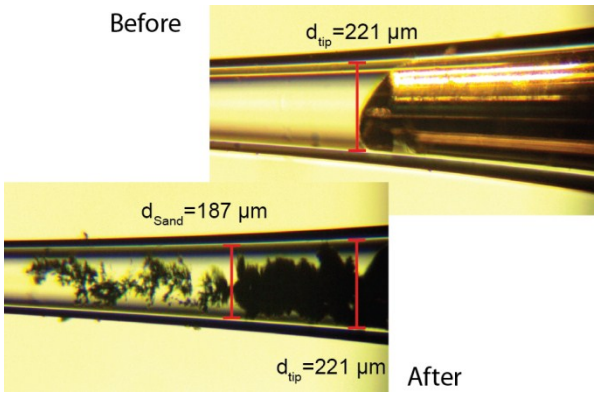

Figure S2. Example of the diameter measurement. J_{tip}=2.61 mA cm^{-2}

Table S1. Total current and the corresponding current density of the capillary cell experiments.

c_0 / mol l^{-1}	I / µA	d_{tip} / µm	d_{Sand} / µm	J_{tip} / mA cm^{-2}	J_{Sand} / mA cm^{-2}	J_{avg} / mA cm^{-2}	t_{Sand} / s
0.5	0.3	272	243	0.52	0.65	0.58	7953
	0.7	302	277	0.98	1.16	1.07	2750
	1.2	316	314	1.53	1.55	1.54	1500
	1.2	277	266	1.99	2.16	2.08	1130
	2	316	247	2.55	4.18	3.36	893
	2.6	286	277	4.05	4.32	4.18	530
	2.7	230	216	6.50	7.37	6.94	300
	5	252	228	10.03	12.25	11.14	235
1	0.5	242	181	1.09	1.94	1.52	6780
	0.7	229	191	1.70	2.44	2.07	5600
	1.4	287	253	2.17	2.79	2.48	3100
	1	221	187	2.61	3.64	3.13	2690
	1.4	251	213	2.83	3.93	3.38	2005
	2.6	321	263	3.21	4.79	4.00	1880
	2.5	266	240	4.50	5.53	5.01	1100
	4	291	249	6.02	8.22	7.12	730
	5.8	330	262	6.78	10.76	8.77	610
2	0.9	233	161	2.11	4.42	3.27	7986
	2	285	236	3.14	4.57	3.86	4055
	2.2	271	173	3.82	9.36	6.59	3537
	2.7	264	182	4.93	10.38	7.66	2224
	4.5	284	215	7.11	12.40	9.75	1316
	4	235	169	9.23	17.84	13.53	868
	7.5	277	207	12.45	22.30	17.37	664

The three kinds of current densities all produce similar scaling for each concentration. In this paper, we only use the one at the initial position of the electrode, i.e. J_{tip}, for all analyses.

Experimental Observation of Electro-osmotic Flow

While electro-osmotic (EO) flow is not significant in practical batteries using dense porous separators, the analysis presented here confirm that EO convection is the primary reason for the observed deviation from the theoretical scaling of Sand's time with current. Thanks to the small lithium debris produced during cell assembly, we are able to observe the fluid velocity in various locations of the capillary to obtain a rough estimation of the Peclet number, which measures the importance of convection relative to diffusion.

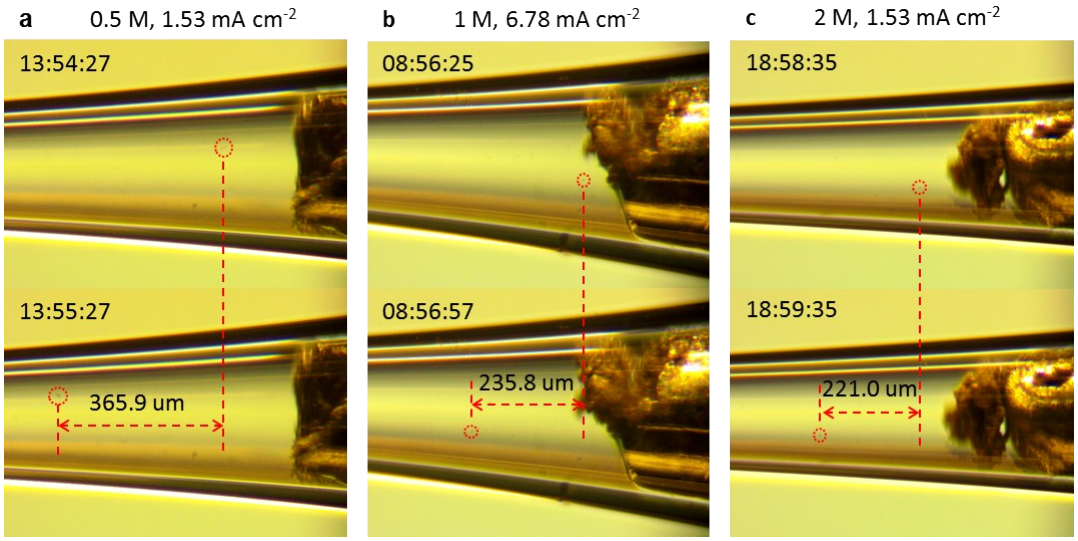

Figure S3. Estimation of the local fluid velocity from floating lithium debris in the capillaries. Also see movies S3-S5.

Table S2. Estimation of the experimental Peclet numbers.

c_0 (mole l^{-1})	J_{tip} (mA cm^{-2})	Δt (s)	ΔL (um)	U (um s^{-1})	d (um)	D (cm^2 s^{-1})	Pe=Ud/D
0.5	1.53	60	366	6.10	286	3.4×10^{-6}	5.13
1.0	6.78	32	236	7.38	330	3.0×10^{-6}	8.12
2.0	3.82	60	221	3.68	235	1.7×10^{-6}	5.09

For the above three experiments that most clearly show convection, the Peclet numbers based on direct observations of the fluid velocity are calculated in Table S2. Values larger than one indicate significant convection, which is neglected in the classical derivation of Sand's time.

Effects of Electro-osmotic Convection on the Apparent Diffusivity

Naively, convection would be expected to enhance mass transfer and thus increase Sand's time compared to pure diffusion, but the coupled problem of EO flow and concentration polarization is very complicated, even in steady state, and has never been analyzed under transient conditions. It is also possible that convective mixing will lower the local "bulk" concentration outside the diffusion layer, thus decreasing Sand's time, and increasing the apparent diffusivity from Sand's formula, as observed in our experiments discussed in the main text. Here, we briefly attempt to estimate the effect of EO convection on the apparent diffusivity from Sand's formula, just to show that this is a plausible explanation of the data, in light of the observed flows and Peclet numbers larger than one shown above.

EO flow in a closed capillary (or porous medium) leads to pressure-driven backflow, in order to maintain zero average flow rate. The sum of EO plug flow driven by the surface double layers and parabolic Poiseuille flow in the opposite direction yield vortices of flow, which have previously been observed in thin-gap (microfluidic) copper electrodeposition experiments by Huth et al.[45]. A simple theory to capture the effect of electro-osmotic convection on the effective diffusivity in a capillary based on Taylor dispersion has been proposed by Yaroshchuk et al.[63]:

$$\frac{D_{app}}{D_{app}^0} = 1 + \frac{1}{48}\mathrm{Pe}^2, \quad \mathrm{Pe} = \frac{\epsilon_0 \epsilon_r \zeta RJ}{\eta \sigma D_{app}^0}. \tag{S1}$$

where, $D_{app}^0 = D_{app}(J=0)$ is a reference diffusivity at zero current and the Peclet number is estimated using the Helmholtz-Smoluchowski electro-osmotic slip formula and the mean electric field, equal to the current density divided by the mean local conductivity. Although this theory loses validity above the limiting current in a strongly depleted capillary[46, 63], it should suffice for our analysis of the current-dependence of Sand's time, prior to diffusion limitation and the onset of dendrites.

Following the suggestion of a recent numerical study[54], the apparent diffusivity in Sand's time for a concentrated electrolyte (without convection) may be approximated by using the traditional apparent diffusivity, e.g. measured by linear response to a small current step[42,43], evaluated at an intermediate concentration, such as $c_0/2$.

The electric field and resulting EO flow are the largest in the depleted region close to the electrode as Sand's time is approached, and this is where the strongest convection is observed in the experiments. Thus, we estimate the local conductivity in the EO Peclet number using 1/5 of the bulk salt concentration c_0. The viscosity at this concentration for the electrolyte is taken from the literature[64]. With these crude but reasonable approximations, only ζ potential (a measure of the surface charge of the capillary) is fitted to the experimental data for the apparent diffusivity, extracted from the experimental Sand's time in the main text.

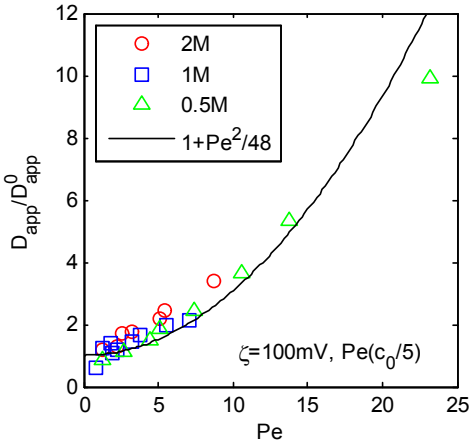

Figure S4. Comparison of the D_{app} obtained from the capillary cells with the Taylor dispersion formula.

Table S3. Parameters used for the Taylor dispersion formula.

c_0 (mol l^{-1})	ϵ_r	ζ (mV)	$^a\eta$ [64] (mPa s)	$^a\sigma_0$ [42] (mS cm^{-1})	D^0_{app} (cm^2 s^{-1})	D_0 [42] (cm^2 s^{-1})	t_{Li} [42]
0.5	35	100	1.35	2.5	0.5×10^{-6}	3.4×10^{-6}	0.38
1	35	100	1.53	4.6	0.7×10^{-6}	3.0×10^{-6}	0.38
2	35	100	2.00	7.7	0.4×10^{-6}	1.7×10^{-6}	0.38

[a]*Evaluated at $c_0/5$.*

This simple theory leads to a reasonable collapse of the experimental data for hydrodynamic dispersion versus Peclet number, as shown Fig. S4. The scaling function lies close to the prediction of Taylor dispersion in the EO vortices observed near the tips. Despite some admittedly very rough approximations, the analysis shows that the observed scaling with current, departing from the classical Sand's formula based on linear diffusion alone, could be attributable

to hydrodynamic dispersion resulting from EO flow in the capillary. This is also consistent with our direct observations of the flow.

An important observation is that the data collapse extrapolates to an apparent diffusivity at zero current that is consistent with literature values for this electrolyte. This means that the results of our capillary experiments, which show noticeable effects of convection at high currents, also have relevance for practical batteries, where EO flow may be negligible. As shown in the main text, the main difference with a theory based purely on diffusion is that the experimentally observed scaling with current is different in the capillary cell. The sandwich cell results (also without significant convection) further confirm the validity of the predicted mechanisms of lithium growth determined by direct visualization in the capillary cell.

Blockage versus penetration of lithium deposits in sandwich cells

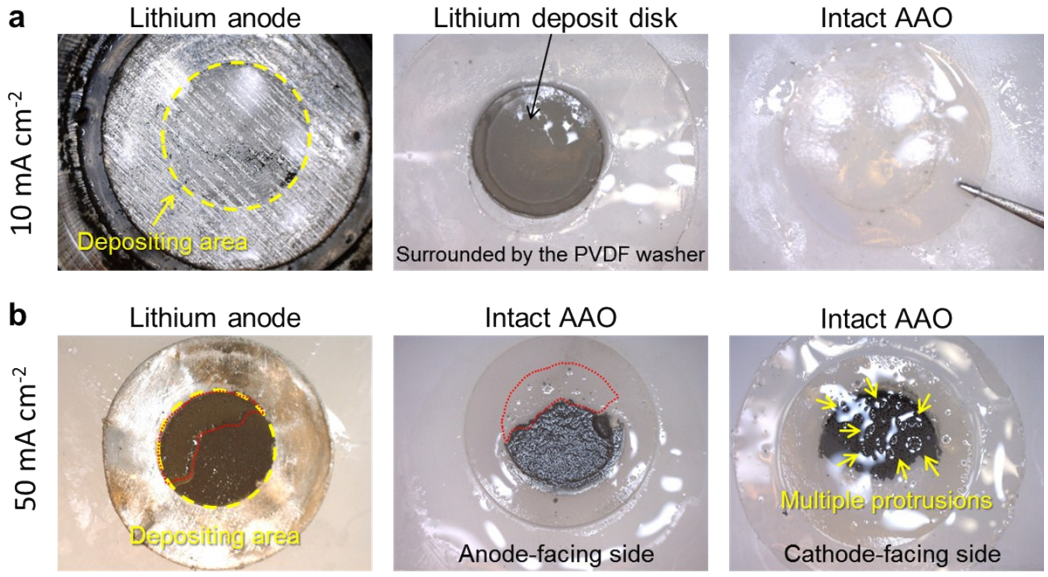

Figure S5. Digital photos of the lithium electrodes, deposits and anodic alumina oxide (AAO) separators harvested from the sandwich cells experiments shown in Fig. 3. In contrast to the clear AAO (a), penetration of AAO by lithium deposits is clearly visible in the case of overlimiting-current deposition (b).

Derivation of the scaling function $f(\tilde{J})$ for the dilute binary electrolyte

Methods of solving diffusion equations can be found in many text books on transport phenomena. Here, we provide an example of derivation to get the scaling function $f(\tilde{J})$.

In a dilute binary electrolyte, the single salt dissociates into equal numbers of anions and cations, i.e. $c_a=c_c=c$, with the charge numbers $z_c=-z_a=1$. Neglecting the convection, the evolution of the concentrations in a one-dimensional system can be modeled by the following set of equations[21],

$$\frac{\partial c}{\partial t} = D_a \frac{\partial^2 c}{\partial x^2} + z_a \mu_a F \frac{\partial}{\partial x}\left(c \frac{\partial \phi}{\partial x} \right) \tag{S2}$$

$$\frac{\partial c}{\partial t} = D_c \frac{\partial^2 c}{\partial x^2} + z_c \mu_c F \frac{\partial}{\partial x}\left(c \frac{\partial \phi}{\partial x} \right) \tag{S3}$$

where D_i and μ_i are diffusion coefficient and mobility of either the anions or the cations, ϕ is the potential applied to the system to maintain the required current density. Elimination of the potential terms yields an effective diffusion equation[21],

$$\frac{\partial c}{\partial t} = D_{app} \frac{\partial^2 c}{\partial x^2}, \quad with \quad D_{app} = \frac{z_c \mu_c D_a - z_a \mu_a D_c}{z_c \mu_c - z_a \mu_a} \tag{S4}$$

By using the Nernst-Einstein relation, $D_i = RT\mu_i$, we can rewrite the effective diffusivity D_{app} and the transference number as,

$$D_{app} = \frac{2 D_c D_a}{D_c + D_a} \tag{S5}$$

$$t_a = 1 - t_c = \frac{-z_a \mu_a}{z_c \mu_c - z_a \mu_a} = \frac{D_a}{D_c + D_a} \tag{S6}$$

so that $D_{app}=2D_c t_a=2D_a t_c$.

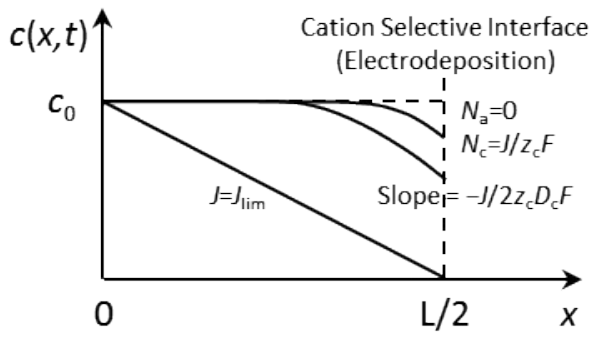

Figure S6. Concentration evolution in the diffusion layer near the surface of the electrode.

We are interested in the concentration evolution near the surface of the electrode when an overlimiting current is applied. From the fact that the current at the boundary (x=L/2) is contributed solely by the electrodeposition of cations, we have the flux of anions as

$$0 = N_a\big|_{x=L/2} = -z_a \mu_a F c \frac{\partial \phi}{\partial x} - D_a \frac{\partial c}{\partial x} \tag{S7}$$

Therefore, the flux of cations at x=L/2 is

$$\frac{J}{z_c F} = N_c\big|_{x=L/2} = -z_c \mu_c F c \frac{\partial \phi}{\partial x} - D_c \frac{\partial c}{\partial x} = -2D_c \frac{\partial c}{\partial x} \tag{S8}$$

from which one can define the limiting current as,

$$J_{\lim} = 2z_c F D_c \frac{c_0}{L/2} = \frac{4z_c c_0 F D_c}{L} = \frac{2z_c c_0 F D_{app}}{t_a L} \tag{S9}$$

We can then use Eqs (S8) and (S9) to obtain the dimensionless boundary condition by scaling c to c_0, x to L/2 and t to $(L/2)^2/D_{\text{app}}$,

$$\frac{\partial \%}{\partial \%} = -J \Big/ \frac{2z_c c_0 F D_{app}}{t_a L} = -J/J_{\lim} = -\%$$ (S10)

To solve the time it takes to deplete the concentration at the surface of the electrode to zero when an overlimiting current is applied, we construct

$$\%(\%,\%) = -\frac{1}{\%} \frac{\partial \%}{\partial \%}$$ (S11)

which should satisfy the linear ambipolar diffusion equation (S4)

$$\frac{\partial \tilde{c}}{\partial \tilde{t}} = \frac{\partial^2 \tilde{c}}{\partial \tilde{y}^2} \tag{S12}$$

where we have applied $\tilde{y} = 1 - \tilde{x}$.

With the following initial and boundary conditions,

$$\tilde{c}(\tilde{y}, \tilde{t} = 0) = 0; \quad \tilde{c}(\tilde{y} = 0, \tilde{t}) = 1 \tag{S13}$$

the dynamics is governed by the complementary error function (erfc) [55],

$$\tilde{c} = \operatorname{erfc}\left(\frac{\tilde{y}}{2\sqrt{\tilde{t}}}\right) \tag{S14}$$

So that,

$$\frac{\partial \tilde{c}}{\partial \tilde{x}} = -\tilde{J}\operatorname{erfc}\left(\frac{1-\tilde{x}}{2\sqrt{\tilde{t}}}\right) \tag{S15}$$

Integration of Eq (S15) and application of the initial and boundary conditions in Eq (S13) yield

$$\tilde{c}(\tilde{x}, \tilde{t}) = 1 - 2\sqrt{\tilde{t}}\,\tilde{J}\operatorname{ierfc}\left(\frac{1-\tilde{x}}{2\sqrt{\tilde{t}}}\right) \tag{S16}$$

where the iterated integral of complementary error function (ierfc) is defined as,

$$\operatorname{ierfc}(z) = \int_z^\infty \operatorname{erfc}(z)\,dz \tag{S17}$$

$$\operatorname{erfc}(z) = \frac{2}{\pi}\int_z^\infty e^{-s^2}\,ds$$

For $\tilde{J} > 1$, the Sand's time can be solved via Eq (S16) at zero concentration,

$$\tilde{c}(\tilde{x} = 1, \tilde{t} = \tilde{t}_{Sand}) = 1 - 2\sqrt{\tilde{t}_{Sand}}\,\tilde{J}\operatorname{ierfc}(0) = 0 \tag{S17}$$

Using ierfc(0) = $\pi^{-0.5}$, the final form of the scaling function is obtained,

$$\tilde{t}_{Sand} = f_{dilute}(\tilde{J}) = \frac{\pi}{4\tilde{J}} \tag{S18}$$

Capillary cell experiments with ether-based electrolytes

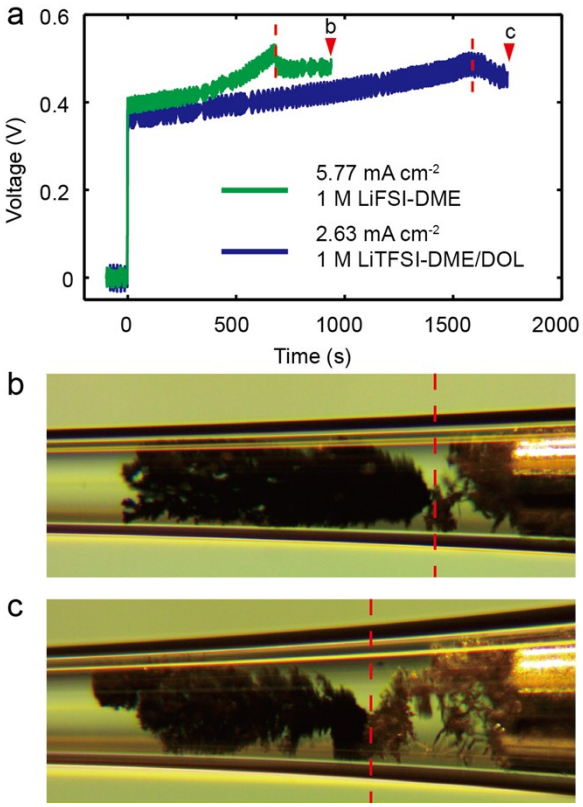

Figure S7. Transition from mossy lithium (collection of root-growing whiskers) to tip-growing fractal lithium in ether-based electrolytes. (a) Voltage responses of the constant-current electrodepositions. Final snapshots of lithium deposits in (b) 1 M LiFSI-DME electrolyte and (c) 1 M LiTFSI-DME/DOL electrolyte. Corresponding movies S6 and S7 are available in the online electronic supplementary information. While the dynamics are similar to those in carbonate-based electrolytes, the differences in the appearance are attributable to the different SEI layers formed in ether-based electrolytes.

References (continued)

63. A. Yaroshchuk, E. Zholkovskiy, S. Pogodin, V. Baulin, *Langmuir* **27** 11710 (2011).

64. Y. R. Dougassa, J. Jacquemin, L. El Ouatani, C. Tessier, M. Anouti, *The Journal of Physical Chemistry B* **118** 3973 (2014).